Journal of Industrial and Engineering Chemistry 83 (2020) 438–448

Contents lists available at ScienceDirect

Journal of Industrial and Engineering Chemistry

journal homepage: www.elsevier.com/locate/jiec

Fibrous network of highly integrated carbon nanotubes/MoO_3 composite bundles anchored with MoO_3 nanoplates for superior lithium ion battery anodes

Se Hwan Oh[a], Seong Mi Park[a], Dong-Won Kang[b,*], Yun Chan Kang[c,*], Jung Sang Cho[a,*]

[a] Department of Engineering Chemistry, Chungbuk National University, Gaesin-Dong, Seowon-Gu, Cheongju-Si, Chungcheongbuk-Do, 361-763, Republic of Korea
[b] School of Energy Systems Engineering, Chung-Ang University, Seoul, 06974, Republic of Korea
[c] Department of Materials Science and Engineering, Korea University, Anam-Dong, Seongbuk-Gu, Seoul, 136-713, Republic of Korea

ARTICLE INFO

Article history:
Received 11 September 2019
Received in revised form 27 November 2019
Accepted 15 December 2019
Available online 8 January 2020

Keywords:
MoO_3
CNTs
Lithium ion batteries
Anode materials
Electrospinning

ABSTRACT

Fibrous network of highly-integrated CNTs/MoO_3 composite bundle in which CNTs anchored with MoO_3 nanoplates was prepared by electrospinning process and subsequent simple heat-treatment. By performing the pre-acid-treatments of both CNTs and PAN, dipole-dipole interactions and hydrogen bonding between CNTs and PAN could form $MoO_2(acac)_2$-PAN-CNTs complex in a solution, which allows for the formation of a stable jet during electrospinning. Notably, by selectively removing PAN in as-spun fibers during heat-treatment, a highly integrated CNTs/MoO_3 bundle network anchored with MoO_3 nanoplates was obtained. This unique CNTs/MoO_3 percolation network makes it possible to achieve a superior lithium ion storage performance by improving electrical conductivity and structure stability. Thus, the unique nanostructure has high discharge capacities of 972 mA h g^{-1} after 100 cycles at 1.0 A g^{-1} and 905 mA h g^{-1} after 800 long-term cycles at 2.0 A g^{-1}, when applied as anode materials for lithium-ion batteries. The discharge capacities of 980, 920, 819, 742, 599, 484, and 374 mA h g^{-1} were observed at current densities of 0.5, 1.0, 2.0, 3.0, 5.0, 7.0, and 10.0 A g^{-1}, respectively.

Introduction

High energy, power density, and long cycle life time of Li-ion batteries (LIBs) have been considered as key issues with the increasing demand for large-scale energy storage such as electric vehicles (EVs), hybrid electric vehicles (HEVs), and smart grids [1–3]. Therefore, unceasing efforts have been made to design and synthesize anode materials with excellent Li ion storage properties for LIBs by various nanostructuring strategies [4–6]. Sophisticated-designed nanostructured anode materials are the fundamental approach for enhancing LIBs performance because these provide a large contact area with the electrolyte, possess short lithium and electron pathways, and can accommodate strain during cycles [7–9]. Another effective strategy for high performance anodes is to composite transitional metal oxides with carbonaceous materials such as graphite, amorphous carbon, carbon nanotube (CNT), and graphene. These carbonaceous materials could compensate the low electrical conductivity of metal oxides anodes and accommodate the large strain induced by Li ion diffusion during cycling [10–13].

Among carbonaceous materials, CNTs are representative candidates for use in LIBs due to their unique electrochemical properties. CNTs have been reported to have a very high electrical conductivity of 10^7 S m^{-1} [14]. Additionally, the high aspect ratio of CNTs compared to the other carbons such as carbon black and graphite, enables to establish an electrical percolation network by incorporating CNTs with a lower weight loading as a composite material [15–17]. It could enable the penetration of liquid electrolyte easily into the structure during cycles, which promotes the electrochemical reaction of host materials. Therefore, various structured CNT- metal oxide composites like as yolk-shell CNT-(NiCo)O/C microsphere [18], SnO_x embedded in carbon nanofiber/carbon nanotube composite [19], Three-dimensional interconnected network GeO_x/CNTs composite spheres [20], CNT-C@TiO_2 composites with 3D networks [21], Mesoporus TiO_2 spheres interconnected by CNT [22], as anode materials have been introduced for LIBs. Although, numerous CNT composite materials

* Corresponding authors.
E-mail addresses: kangdwn@cau.ac.kr (D.-W. Kang), yckang@korea.ac.kr (Y.C. Kang), jscho@cbnu.ac.kr (J.S. Cho).

https://doi.org/10.1016/j.jiec.2019.12.017
1226-086X/

were proposed as anodes, the capacity and cycling stability are still not quite satisfactory for practical use. It is due to the non-uniform distribution of CNTs caused by van der Waals forces, phase segregation between metal oxides, and an insufficient amount of CNTs composited with metal oxides.

Recently, molybdenum trioxides (MoO_3) have been considered as promising anodes for electrochemical energy storage devices owing to their high theoretical specific capacity of 1117 mA h g^{-1} and high stability with a layered structure [23]. Each layer is composed of two sub-layers, each of which is formed by corner-sharing octahedra along [001] and [100]; the two sub-layers stack together by sharing the edges of the octahedra along [001]. An alternate stack of these layered sheets along [010] would lead to the formation of MoO_3, where a van der Waals interaction would be the major binding force between the piled sheets. Therefore, stable layered MoO_3 structure is able to act as temporary support for the intercalation of lithium ions during charge/discharge process [23,24]. Furthermore, MoO_3 as an environmentally friendly n-type semiconductor material with a band gap of 3.1 eV is a highly attractive anode material due to its high electrical conductivities compare to other metal oxides [25,26].

In this study, we proposed for the first time a unique fibrous network of highly-integrated CNTs/MoO_3 composite bundle anchored with MoO_3 nanoplates for anodes in LIBs. By performing the pre-acid-treatments of both CNTs and PAN, dipole-dipole interactions and hydrogen bonding between CNTs and PAN could form $MoO_2(acac)_2$-PAN-CNTs complex, which allows for the formation of a stable jet during spinning. As a result, fibrous network of highly-integrated CNTs without being aggregated was successfully obtained after electrospinning process. Subsequently, the amorphous carbon with lower electrical conductivity compared to CNTs, induced by PAN decomposition was selectively removed during the heat-treatment. The highly integrated CNTs/MoO_3 composite bundle constitute network and these are efficiently interconnected each other and also contacted with MoO_3 nano-plates. As a consequence, high reversible capacity, long cycle life stability, and superior rate properties of anodes could be achieved using the unique nanostructure proposed in this study.

Experimental

Sample preparation

Fibrous network of highly-integrated CNTs/MoO_3 composite bundle anchored with MoO_3 nanoplates or pure MoO_3 flat-rods were prepared by electrospinning process and a subsequent different heat-treatments, respectively. First, the colloidal solution for electrospinning was prepared by dissolving 3.0 g of Mo(III) acetylacetonate [$MoO_2(acac)_2$, Junsei, 98.0%] and 1.5 g of sulfonated polyacrylonitrile [PAN, Mw: 150,000, Sigma-Aldrich] in a mixed solution containing 20 mL of dimethylformamide [DMF, Samchun, 99.8 %] and 1.0 g of acid-treated CNTs. For this purpose, CNTs were modified using HNO_3/H_2SO_4 (1:3 vol %) acid solution at 80 °C and washed using a solution mixed with distilled water and ethyl alcohol. Subsequently, the acid-treated CNTs were freeze-dried. In order to prepare the spinning solution, PAN was also sulfonated beforehand with H_2SO_4 acid solution at 80 °C. The prepared colloidal solution was loaded into a plastic syringe equipped with a 21-gauge stainless steel nozzle. Then, the solution was ejected at a flow rate of 1 mL h^{-1}, the rotation speed of the drum collector was 150 rpm, the distance between the tip and the collector was fixed at 25 cm, and the applied voltage between the collector and the syringe tip was maintained at 12 kV. As-spun precursor $MoO_2(acac)_2$/PAN/CNTs composite nanofibers obtained after electrospinning were stabilized at 100 °C for 3 h under air. Subsequently, composite nanofibers were performed to heat-treatment at various temperatures of 350, 400, and 500 °C, respectively, for 3 h under air. For simplicity, the resulting MoO_3/CNT composite fibrous-networks or MoO_3 plat-rods obtained after heat-treatments at 300 and 400, and 500 °C were denoted to as “A350”, “A400”, and “A500”, respectively.

Characterization techniques

The morphologies of the samples were examined through field-emission scanning electron microscopy (FE-SEM, ULTRA PLUS, ZEISS) and field-emission transmission electron microscopy (FE-TEM, JEOL, JEM-2100 F). The phase analysis was evaluated by X-ray diffractometry (XRD, D8 Discover with GADDS, The Bruker) using Cu K_α radiation (λ = 1.5418 Å). The functional group of the sample was investigated by Fourier transfer infrared (FT-IR) spectra (JASCO FT-IR 480 Plus spectrophotometer). The structure of the carbonaceous materials in the composite were characterized at room temperature via Raman spectroscopy (Jobin Yvon LabRam, HR800, excitation source = 514 nm He–Ne laser). X-ray photoelectron spectroscopy (XPS, Thermo Scientific K-Alpha) with a focused monochromatic Al K_α at 12 kV and 20 mA was used to analyze the composition of the nanofibers. The surface area of the samples was measured using the Brunauer–Emmett–Teller (BET) method with N_2 as the adsorbate gas. Thermogravimetric (TG) analysis was performed using a Pyris 1 TGA (Perkin Elmer) within a temperature range of 25–700 °C at a heating rate of 10 °C min^{-1} under air.

Electrochemical measurements

The electrochemical properties of the samples were measured by assembling 2032-type coin cells. The cell electrodes were prepared using slurry consisting of 70 wt% active anode material, 20 wt% carbon black (Super-P) as a conductive material, and 10 wt% binder composed of sodium carboxymethyl cellulose (CMC) on a copper foil. Lithium metal and microporous poly(propylene) film were used as the counter electrode and separator, respectively. The electrolyte was created by dissolving 1 M $LiPF_6$ in a mixture of fluoroethylene carbonate and dimethyl carbonate (FEC/DMC, 1:1 v/v). The entire cell was assembled in an argon atmosphere in a glove box. The charge/discharge characteristics of the samples were measured at various current densities in the voltage range of 0.001–3.0 V. The size of the negative electrode containing the sample was 1.4 cm × 1.4 cm. Cyclic voltammetry measurements were performed at a scan rate of 0.1 mV s^{-1} between 0.001 and 3.0 V. Electrochemical impedance spectra of samples were analyzed in the frequency range between 0.01 Hz and 100 KHz at room temperature with a signal amplitude of 10 mV.

Results and discussion

Fibrous network of highly-integrated CNTs/MoO_3 composite bundle anchored with MoO_3 nanoplates was prepared by electrospinning process and subsequent simple heat-treatment. The detailed structure formation mechanism of the unique MoO_3/CNT composite fibrous-network was described in Scheme 1. In general, it is difficult to form a stable jet using a solution containing a large amount of CNTs along with PAN and metal precursors during electrospinning, which is due to the CNTs aggregation caused by van der Waals forces and the phase segregation between the precursors in a spinning solution. Therefore, uneven as-spun fibers, in which CNTs are not dispersed well and phase segregated, are obtained after spinning. However, to solve this problem in this study, PAN was pre-sulfonated to attach functional groups of amide (NH_2—C=O) and sulfuric acid (—SO_3H) groups on it. CNTs were also modified to have a carboxyl group attached on that surface. Therefore, dipole–dipole interactions and hydrogen bonding between CNTs and $MoO_2(acac)_2$ were formed.

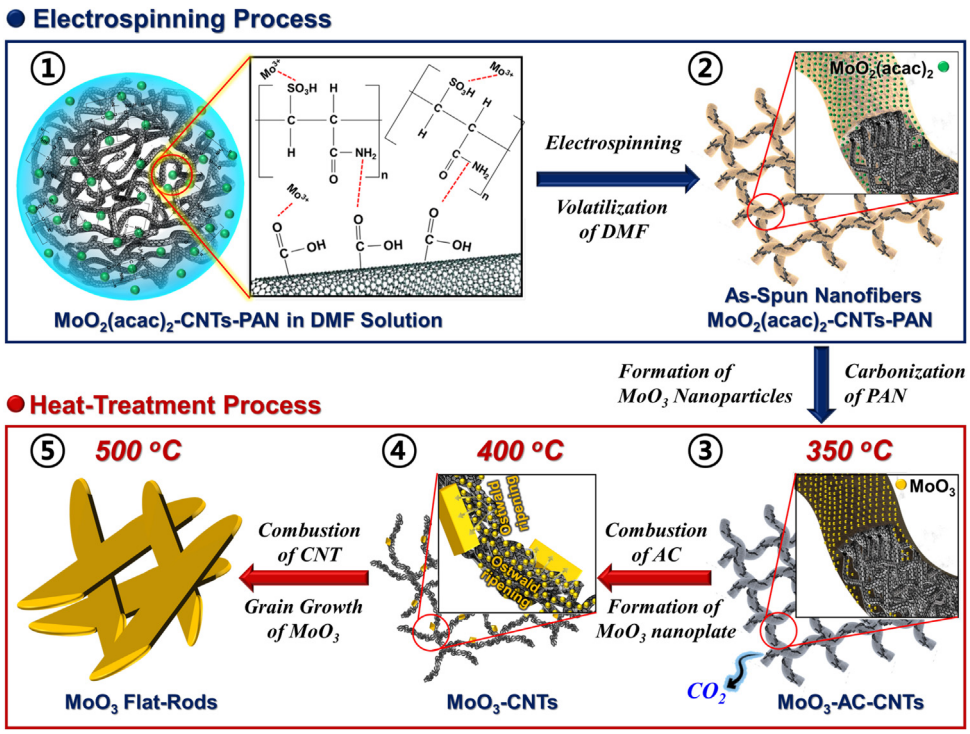

Scheme 1. Formation mechanism for the fibrous network of highly integrated CNTs/MoO_3 composite bundles anchored with MoO_3 nanoplates by electrospinning followed by heat treatment.

Additionally, $MoO_2(acac)_2$ precursor could be adsorbed onto both modified CNTs and sulfonated PAN, resulting uniform complex of $MoO_2(acac)_2$-CNTs-PAN in the DMF colloidal spinning solution (scheme 1 -①). As a result, stable spinning jet containing uniformly distributed $MoO_2(acac)_2$-CNTs-PAN in DMF was generated, which could synthesize the homogeneous one-dimensional structure as a product, in this study. During the electrospinning process, DMF solvent is volatilized from the jet surface at the initial stage of the spinning and solidified to form a $MoO_2(acac)_2$-CNTs-PAN nanofibers (scheme 1 -②). Subsequently, PAN in the composite was carbonized and concurrently, $MoO_2(acac)_2$ precursor also decomposed and crystalized into MoO_3 nanocrystals during the simple heat-treatment, which therefore, formed low crystalline MoO_3-CNTs composite nanofibers containing amorphous carbon (scheme 1 -③). When the heat treatment further progress on, the amorphous carbon induced by PAN decomposition was selectively removed from the composite nanofibers into CO_2 gas. Additionally, MoO_3 nanoparticles grain-grew into the MoO_3 nanoplates. As a result, fibrous network of CNTs/MoO_3 composite bundle anchored with MoO_3 nanoplates was finally prepared, in which a highly integrated CNTs bundle and MoO_3 nanoparticles constitute the nanofiber matrix and these are efficiently interconnected each other as a network and also contacted with MoO_3 nanoplates, in Scheme 1-④. After heat-treatment at higher temperature above 500 °C, CNTs bundle in the composite were combusted and at the same time, MoO_3 nanoplates were grown in the c-axis direction, resulting pure MoO_3 flat-rods.

The formation mechanism of each nanostructure described above was investigated in detail by tracing both the morphology and phase of the samples at each step. As-spun nanofibers obtained after electrospinning process were shown in Fig. 1. From the FE-SEM image in Fig. 1a, uniform one-dimensional nanostructure with a mean diameter of 350 nm was successfully obtained. The uniformly structured nanofibers prove that the starting materials of both CNTs and PAN successfully distributed well with $MoO_2(acac)_2$ in DMF solvent by acid-treatments before spinning, which results stable jet during the electrospinning process. Therefore, highly integrated and interconnected CNTs were confirmed at the fractured nanofiber surface in Fig. 1b. On the other hand, the as-spun fibers obtained from a solution using CNTs and PAN without acid-treatments showed aggregated and uneven nanofiber structure, as shown in Fig. S1. From the FT-IR result of as-spun nanofibers (Fig. 1c), the peaks located at 588, 1040, 1197 and 1214 cm^{-1} reveals the presence of N—H, C—S, O=S=O, and C—N, respectively, which are the characteristic peaks of sulfonated polyacrylamide groups (-SO_3H, O=C—NH_2) formed at the acid-treated PAN [27,28]. Additionally, the peaks at 1580 cm^{-1} (C=O) and 3400 cm^{-1} (O—H) showed the formation of carboxylic acid (—COOH) group at the CNTs surface. The dipole-dipole interactions and hydrogen bonding between CNTs and PAN could form $MoO_2(acac)_2$-PAN-CNTs complex [29–31]. The thermogravimetric analysis (TGA) curve of as-spun nanofibers shown in Fig. 1d revealed a three-step weight loss. The first weight loss at around below 200 °C is attributed to the evaporation of adsorbed water molecules in the composite [32]. The carbonization of PAN and following decomposition of the carbon and the decomposition of $MoO_2(acac)_2$ were occurred at the second step between 200 °C and 400 °C. Finally, CNTs in the composite started to combust at around 450 °C. From the TGA result, it is proved that by controlling the temperature during heat-treatment, only the amorphous carbon could be selectively removed while leaving the CNTs in the composite, which is the key to prepare the unique fibrous network of CNTs/MoO_3 composite bundle anchored with MoO_3 nanoplates, in this study.

In order to convince the morphological change by the order of combustion between amorphous carbon and CTNs, heat-treatment of as-spun nanofibers were performed at 350 °C, as shown in Fig. 2. At the relatively low temperature of 350 °C, PAN which has a decomposition temperature of 230 °C in the composite was carbonized. Therefore, it is obviously observed that the CNTs were exposed to the nanofiber surface as indicated by the arrows in Fig. 2c. From the high-resolution (HR) TEM observation in Fig. 2d,

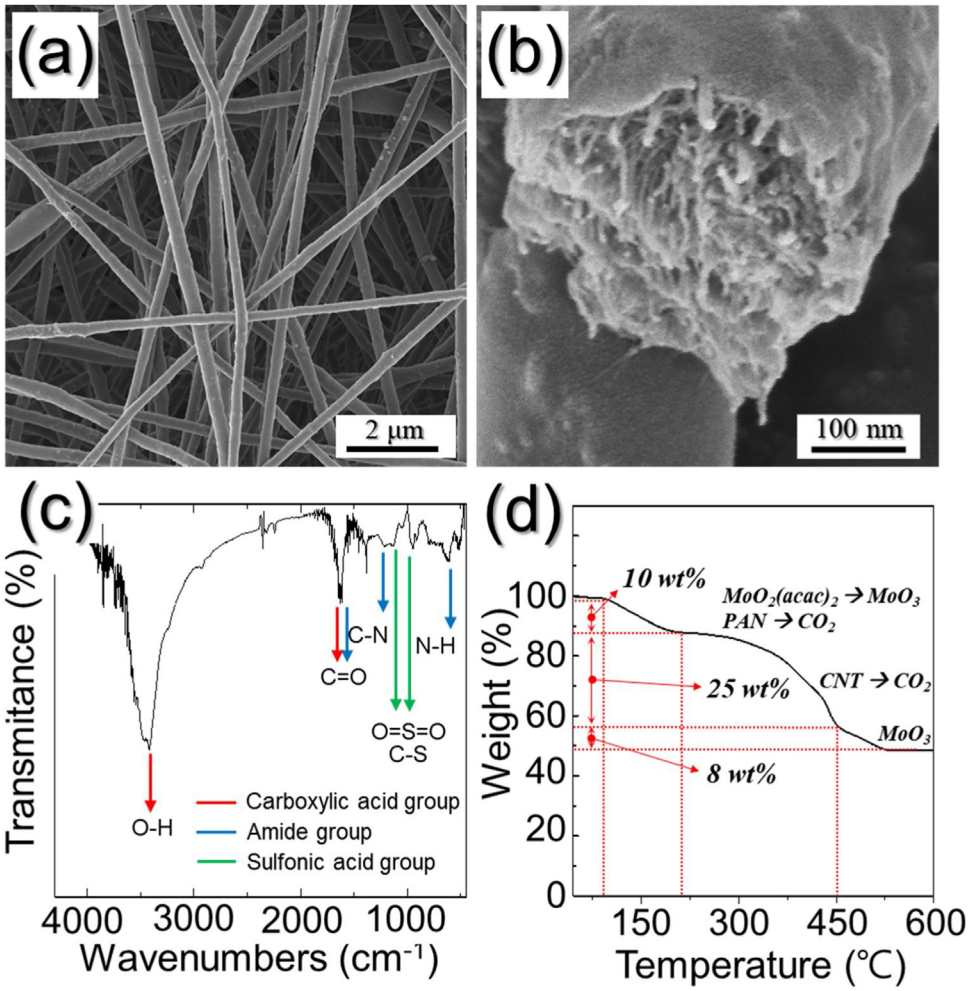

Fig. 1. (a,b) FE-SEM images, (c) FT-IR spectrum, and (d) TGA curve of as-spun $MoO_2(acac)_2$-CNT-PAN composite nanofibers obtained after electrospinning process.

the clear lattice fringes separated by 0.34 nm corresponding to the (002) crystal planes of CNTs were confirmed. However, it was difficult to confirm the lattice fringes of MoO_3 crystals, which is because amorphous-like MoO_3 were formed during the heat-treatment at the low temperature of 350 °C. Therefore, pale-ring patterns representing MoO_3 nanocrystals and (002) plane pattern of CNTs were both confirmed in the selected area electron diffraction (SAED) pattern in Fig. 2e [33]. The XRD pattern of the composite also showed the amorphous-like broad diffraction pattern, as shown in Fig. 2f. However, the formation of MoO_3 phase in the structure after heat-treatment at 350 °C could be confirmed form the binding energies for Mo 3d and O 1s in XPS spectra (Fig. S3). The elemental mapping images shown in Fig. 2g indicated the existence of molybdenum, oxygen, and carbon uniformly distributed in the structure, which reveals the homogeneously distribution of the low-crystalline MoO_3 nanocrystals in the matrix composing CNTs and carbon. From the TGA curve of the composite in Fig. S4a, 26 wt% weight loss was confirmed due to the decomposition of carbon derived from PAN and CNTs.

In order to improve the lithium ion storage property of the MoO_3/CNTs/amorphous carbon composite nanofibers as anode materials, heat-treatment at 400 °C was performed to selectively remove the amorphous carbon derived from PAN with relatively lower electrical conductivity compared to CNT. Therefore, the obtained fibrous network of CNTs/MoO_3 composite bundle anchored with MoO_3 nanoplates after heat-treatment at 400 °C were shown 2-dimensional nanostructure and these established an electrical percolation network due to selectively decomposition of amorphous carbon surrounding CNTs in the composite, as shown in Fig. 3a–d. CNTs networks contribute to the high electrical conductivity of anodes, in Fig. 3a. During heat-treatment, some of MoO_3 nanocrystals located at the nanofiber surface grain-grew and became MoO_3 nanoplate anchored in CNT bundle matrix, as shown in Fig. 3b,c. In particular, the highly integrated and interconnected CNTs bundles constitute a one-which provides a conductive pathway for electrons generated from MoO_3 nano-plates and enables rapid charge/discharge during cycling. Concurrently, this unique percolation structured network enables the penetration of liquid electrolyte into the structure easily, which would promote the electrochemical reaction during cycles. From the HR-TEM image in Fig. 3e, the clear lattice fringes separated by 0.34 nm corresponds to the (002) crystal planes of CNTs [33]. Additionally, the lattice fringe separated by 0.35 nm in the nano-plate was due to the (040) crystal plane of MoO_3 as shown in Fig. 3f [34,35]. The presence of MoO_3 was further verified by XRD (Fig. 3g) and SAED (Fig. 3h) patterns, in which the sharply defined XRD pattern and clear ring SAED patterns, both represent the MoO_3 nanocrystals and CNTs. By applying the Scherrer equation to the characteristic peaks of hexagonal MoO_3 in the XRD pattern, the mean crystallite size of the MoO_3 nanoplates was calculated as 24.4 nm. Elemental mapping images shown in Fig. 3i indicated that the CNTs fibrous networks were composited with MoO_3 nanocrystals as a bundle and the network was anchored with MoO_3 nano-plates.

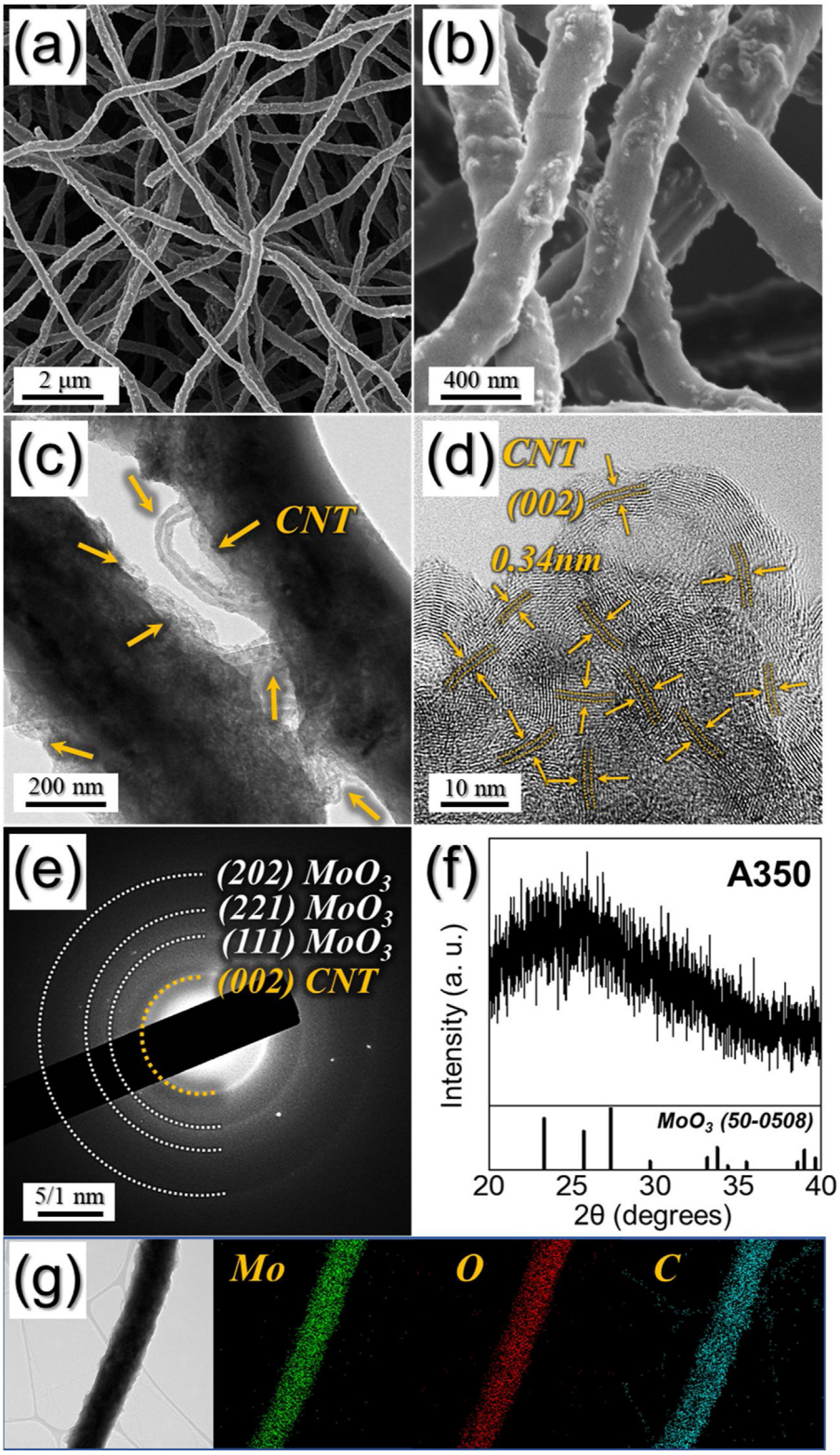

Fig. 2. Morphologies, SAED, XRD patterns, and elemental mapping images of A350 sample: (a and b) FE-SEM images, (c) TEM image, (d) HR-TEM image, (e) SAED pattern, (f) XRD pattern, and (g) elemental mapping images.

The chemical state of the fibrous network of CNTs/MoO_3 composite bundle anchored with MoO_3 nanoplates obtained after heat-treatment at 400 °C was analyzed by XPS as shown in Fig. 4. The survey spectrum of the composite in Fig. 4a showed the peaks corresponding to Mo 3d, C 1s, and O 1s. The Mo 3d spectrum in Fig. 4b had intense peaks centered at 232.6 for Mo $3d_{5/2}$ and 235.7 eV for Mo$3d_{3/2}$; the peaks are corresponding to Mo^{6+}, which proves the formation of MoO_3 [36,37]. Additional peaks at 231.6 and 234.7 eV revealed Mo^{5+}, which are attributed to the oxygen vacancies of MoO_3 crystals due to the non-stoichiometry of MoO_3 surface [38,39]. The C 1s spectrum in Fig. 4c consists of three peaks located at 284.29 eV (C—C/C=C), 285.47 eV (C—O), and 288.25 eV (C=O)

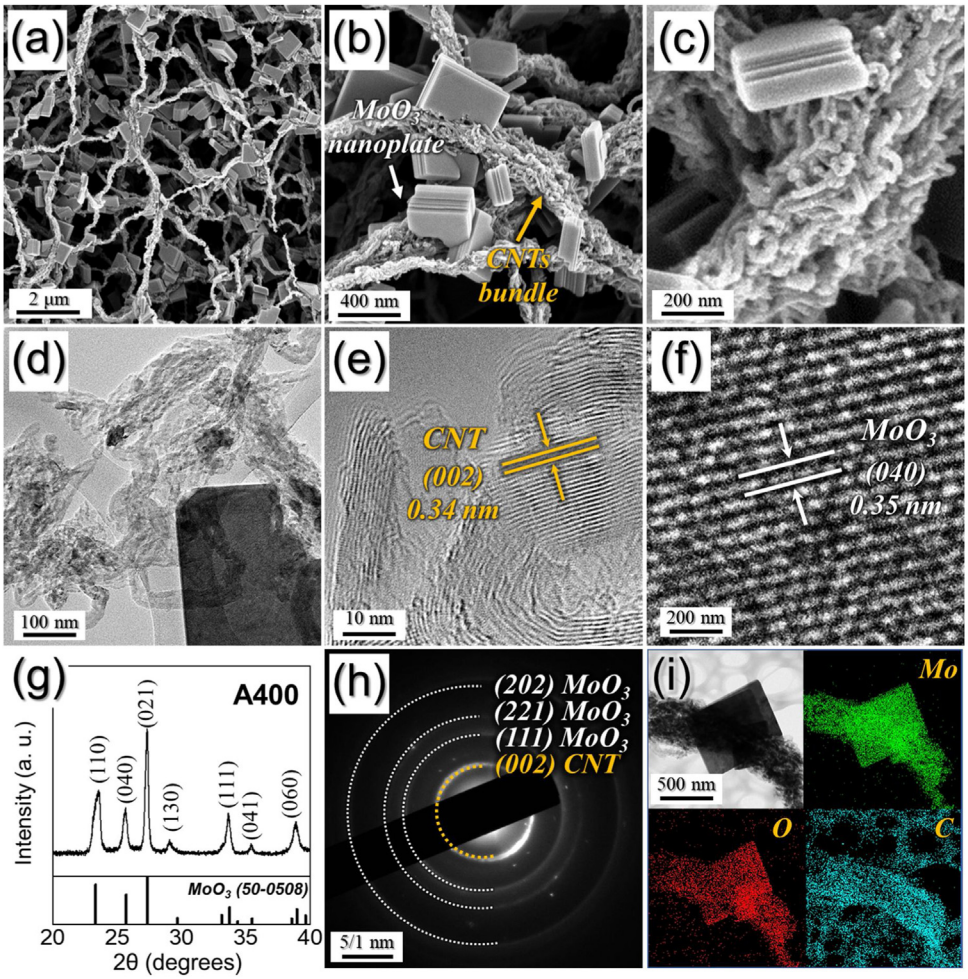

Fig. 3. Morphologies, XRD, SAED patterns, and elemental mapping images of A400 sample: (a–c) FE-SEM images, (d) TEM image, (e,f) HR-TEM images, (g) XRD pattern, (h) SAED pattern, and (i) elemental mapping images.

[40,41]. The sharp peak of C—C/C=C bond is due to the highly integrated CNTs, which leads to high electrical conductivity of the MoO_3/CNT composite. The Raman spectrum (Fig. 4d) was composed of five strong resonance peaks located at 335, 469, 665, 819, and 994 cm^{-1} in the range of 300–1000 cm^{-1}, which are attributed to O—Mo—O bending mode, O—Mo—O asymmetric stretching/bending mode, Mo_3—O stretching mode, Mo_2—O stretching mode, and Mo^{6+}=O stretching mode, respectively [42,43]. These peaks are in good agreement with the results previously reported in the literatures for MoO_3 [42,43]. Additionally, D- (~1345 cm^{-1}) and G-bands (1593 cm^{-1}), which are commonly observed for graphitic carbon with defects were detected [44]. The intensity ratio value of the D to G bands (I_D/I_G), which is commonly used as a measure with regard to defects and disorders in graphitic materials, was approximately 1.16 for the fibrous network of CNTs/MoO_3 composite bundle anchored with MoO_3 nanoplates obtained after heat-treatment at 400 °C. This I_D/I_G value is lower than that of the MoO_3/CNT/amorphous carbon composite obtained at 350 °C (the I_D/I_G value of A350 is 1.28 in Fig. S5), implying that the amorphous carbon derived by PAN was selectively removed from the composite while leaving the CNTs in the composite during the heat-treatment at 400 °C. Another D′ band at around 1620 cm^{-1} was also observed due to the defects in CNTs, which could be attributed to the existence of substitutional heteroatom vacancies or other defects on CNT-walls formed by during acid treatment of CNTs and heat treatment of 400 °C [45]. Fibrous network of CNTs/MoO_3 composite bundle in which CNTs anchored with MoO_3 nanoplates was 16 wt%, which is calculated based on the weight loss at around 450 °C in the TGA results (Fig. S7).The sample obtained after heat-treatment at the highest temperature of 500 °C were shown in Fig. 5. The overall morphology of the sample was changed to flat-rods, in which the average length and thickness of the flat-rods were 3 μm and 100 nm, respectively (Fig. 5a). After heat-treatment at the high temperature above 500 °C, CNTs bundle in the composite were totally combusted and at the same time, MoO_3 nano-plates were grown in the c-axis direction, resulting pure MoO_3 flat-rods. The clear lattice fringe separated by 0.35 nm in the flat-rods was corresponding to the (040) crystal plane of MoO_3 in Fig. 5c [34,35]. The XRD and SAED patterns in Fig. 5d,e showed the (002), (202), and (200) crystal planes of MoO_3, which further prove the formation of pure MoO_3 phase. Elemental mapping images in Fig. 5f also indicates that the flat-rods were composed solely of MoO_3 without any carbonaceous materials. The PAN and CNTs in the as-spun fibers were completely removed in the structure during the heat-treatment at 500 °C, which is also evidenced by the TGA curve, in which the weight loss does not appear (Fig. S4b). The Brunauer–Emmett–Teller (BET) surface areas of each sample obtained after heat-treatment at 350, 400, and 500 °C were 9.8, 42.3, and 0.8 $m^2 g^{-1}$, respectively (Fig. S9). Among samples, the highest BET surface area of A400 might be due to the unique percolation network structure, in which meso-pores between CNT/MoO_3 composite bundles contributed to the high BET value of the fibrous network of CNTs/MoO_3 composite.

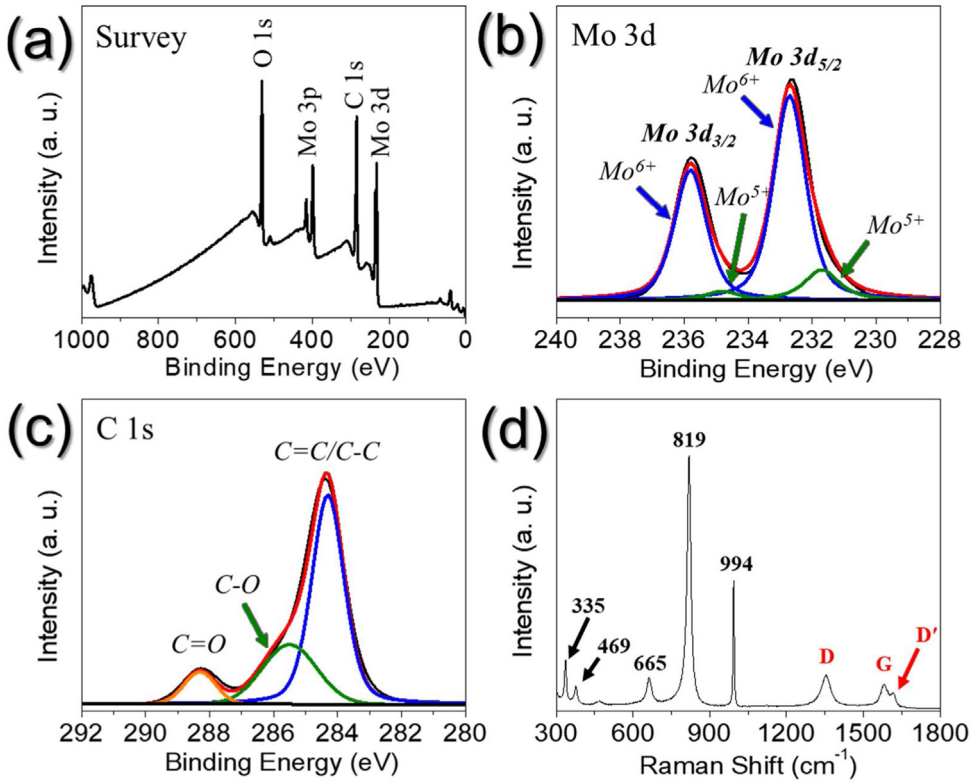

Fig. 4. (a) Survey XPS, (b) Mo 3*d* XPS, (c) C 1*s* XPS, and (d) Raman spectra of A400 sample.

The lithium ion storage properties of the samples obtained at various heat-treatment temperatures of 350, 400, and 500 °C were investigated in Fig. 6. Cyclic voltammetry (CV) curves of A400 obtained at a scan rate of 0.1 mV s^{-1} over a potential range of 0.001–3.0 V were depicted in Fig. 6a. In the first cathodic sweep, irreversible reduction peaks located at 2.73 and 2.25 V were detected, which is attributed to the multistep intercalation processes of Li^+ ions into the crystalline MoO_3 to form Li_xMoO_3 [46–49]. Additionally, the peak at 0.26 V was attributed to the reaction of Li^+ ions and Li_xMoO_3 to form metallic Mo and Li_2O, as well as the co-interaction of the solvated Li or Li^+ ions into CNTs [46–50]. In the anodic scan, the reversible peaks at 1.32 and 1.81 V are attributed to Li^+ ions extractions from sites with different energies as well as phase transition process [46–49]. In the following cycles, redox peak pairs of 0.21/1.32 and 1.51/1.81 were detected, which reveals the reversible phase transitions (monoclinic-orthorhombic-monoclinic) of lithiated Li_xMoO_3 during Li^+ insertion and extraction process, which are in good agreement with previous reports [46–49]. The CV curves of A500 (Fig. S10) also showed the similar shapes with those of A400 (Fig. 6a). However, The shapes for the CV curves of A350 (Fig. S10a) exhibited broad shape which is because A350 is composed of amorphous-like MoO_3 with low crystallite size and amorphous carbon [51,52]. Therefore, the discharge and charge process of the samples could be summarized by Eqs. (1) and (2):

First discharge process:

$$MoO_3 + xLi^+ \rightarrow Li_xMoO_3 \quad (1)$$

Charge-discharge process:

$$Li_xMoO_3 + (6-x)Li^+ + (6-x)e^- \leftrightarrow Mo + 3Li_2O \quad (2)$$

The initial discharge-charge profiles of the samples at a high current density of 1.0 A g^{-1} were shown in Fig. 6b. Although, the discharge profile for A350 did not have a clear plateau, the ones for both A400 and A500 samples clearly exhibited a long and distinctive plateau at around 0.26 V, which coincided with the sharp reduction peaks in the CV curves, as shown in Fig. 6a and S10. The initial discharge capacities of A350, A400, and A500 at a current density of 1.0 A g^{-1} were 1247, 1308, and 1462 mA h g^{-1}, respectively, and their corresponding Coulombic efficiencies were 62, 71, and 72 %. A350 showed the lowest initial Coulombic efficiency, which is attributed to the large amount of amorphous carbon with high irreversible capacity loss and composited with nano-sized MoO_3 crystals. In general, nano-sized active materials show lower initial Coulombic efficiencies due to their large surface area, which leads the formation of solid electrolyte interface (SEI) layer thick on the surface [53].

The cycling performances of A350, A400, and A500 samples at a current density of 1.0 A g^{-1} are shown in Fig. 6c. The A350 and A400 samples showed the excellent cycling performances during 100 cycles despite the high current density. The carbonaceous materials could accommodate the drastic mechanical stress of MoO_3 nanoparticles induced by repeated Li^+ ion diffusion by surrounding them. On the other hand, the discharge capacity of the A500 steadily decreases up to 100 cycles. The capacity fading of A500 is attributed to the structure destruction of the MoO_3 flat-rods with high crystallite size during repeated cycles. The discharge capacities of A350, A400, and A500 samples for the 100th cycle were 578, 972, and 636 mA h g^{-1}, respectively and the corresponding capacity retentions, which were measured from the second cycle, were 76, 99, and 60 %, respectively. Compared to A350 and A400, the lower reversible capacity of A350 is due to the higher carbonaceous materials contents. A400 also showed the excellent rate property, as shown in Fig. 6d. The discharge capacities of 980, 920, 819, 742, 599, 484, and 374 mA h g^{-1} were observed at current densities of 0.5, 1.0, 2.0, 3.0, 5.0, 7.0, and

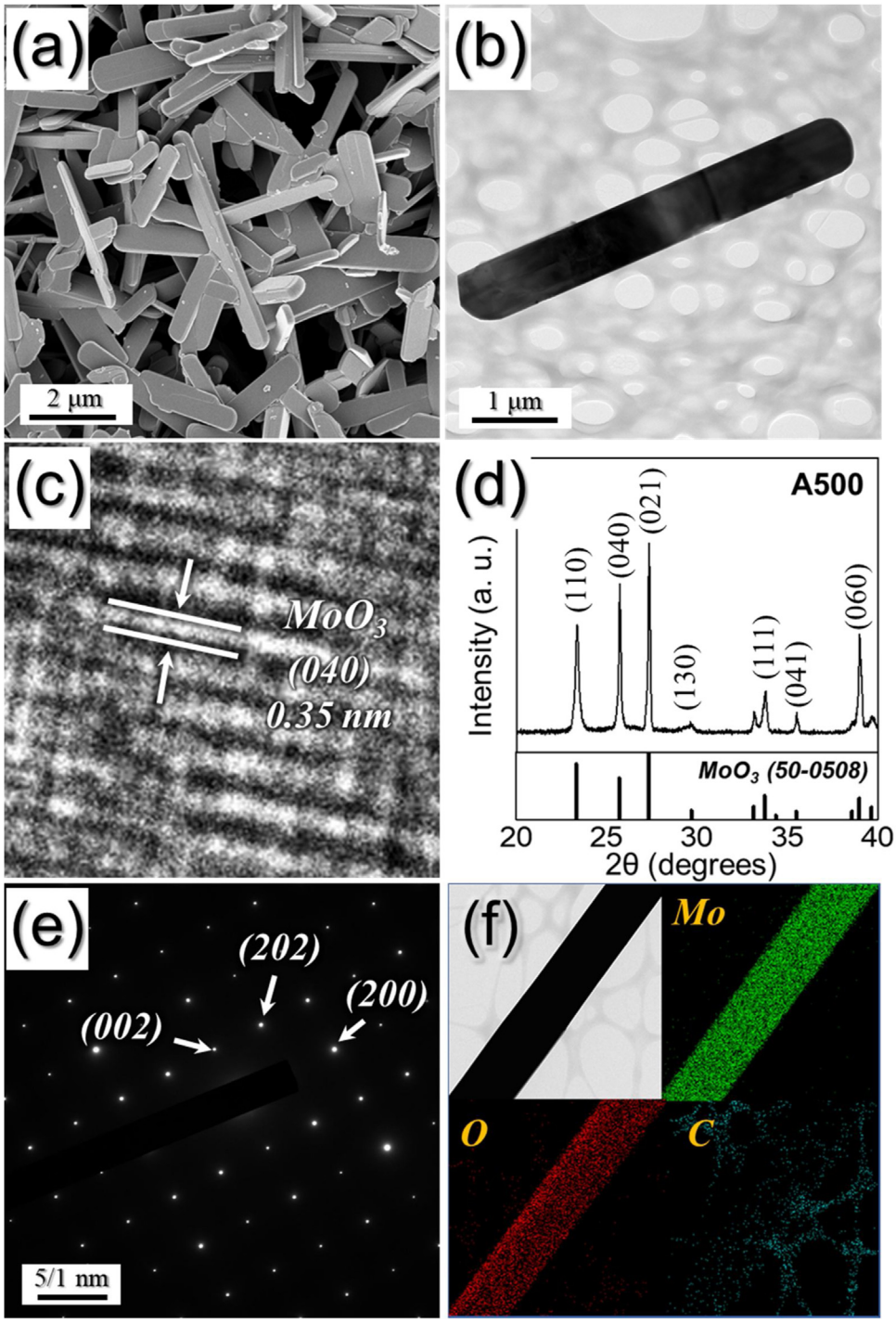

Fig. 5. Morphologies, XRD, SAED patterns, and elemental mapping images of A500 sample: (a, b) FE-SEM images, (c) HR-TEM image, (d) XRD pattern, (e) SAED pattern, and (f) elemental mapping images.

10.0 A g^{-1}, respectively. The highly integrated CNTs bundle network of the composite contributed to the high electrical conductivity, which could facilitate fast electron transfer by improving electrical contact between the active sites and the electrode. Moreover, the CNTs/MoO_3 percolation network formed by selectively decomposition of amorphous carbon surrounding CNTs in the composite enabled the penetration of liquid electrolyte into the composite, which also promoted the electrochemical reaction. Notably, when the current density returned to 0.5 A g^{-1}, the A400 sample recovered a stable discharge capacity of 1020 mA h g^{-1} even after the rate performance test at extremely high current densities implying that the Li^+ ion storage performance of the fibrous network of CNTs/MoO_3 composite bundle anchored with MoO_3 nanoplates was not degraded at high current densities. Fig. 6e shows the long-term cycle performance of the A400 sample at a high current density of 2.0 A g^{-1}. It exhibited a discharge capacity of 1163 mA h g^{-1} in the first cycle, and good cycling stability with a discharge capacity of 905 mA h g^{-1} after 800 cycles. Additionally, it showed a decent Coulombic efficiency of almost 100 % during the long-term cycling. The high structural stability of the A400 during repeated charge discharge processes resulted in excellent long-term cycling performance of the fibrous CNTs/MoO_3 composite network.

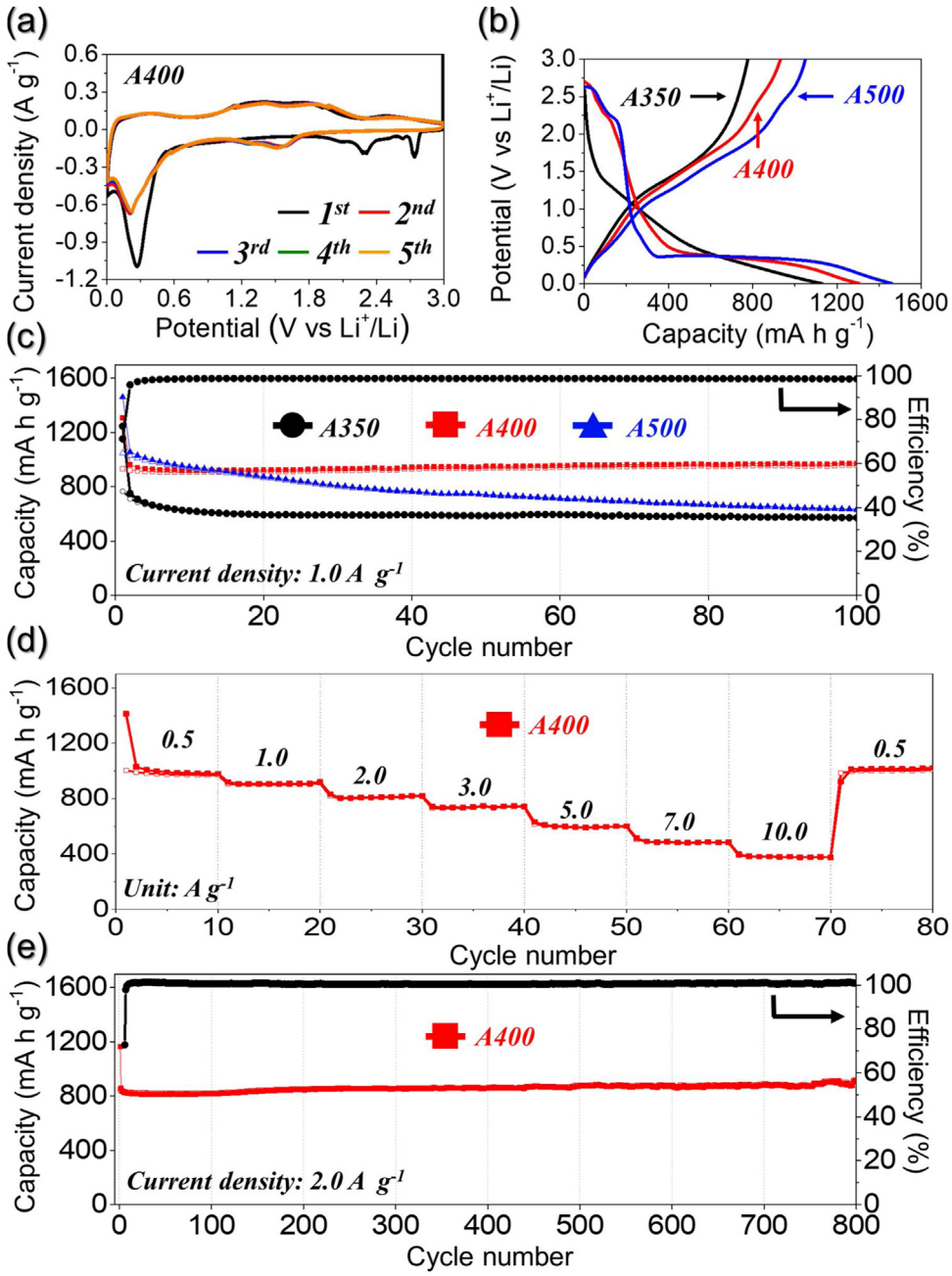

Fig. 6. Electrochemical properties of A350, A400, and A500 samples: (a) CV curve of A400, (b) initial discharge-charge profiles, (c) cycling performances, (d) rate performance of A400, and (e) long-term cycling performance of A400.

In order to calculate the capacity contribution of the CNT framework to the A400 electrode, A400 was etched with NH_4OH solution to obtain pure CNT nanofibers. The first discharge–charge profiles confirmed that the CNT framework was pure carbon with discharge and charge capacities of 681 and 398 mA h g^{-1}, respectively, as shown in Fig. S11a. The pure CNT framework exhibited a reversible discharge capacity of 212 mA h g^{-1} at a current density of 1.0 A g^{-1} for the 50th cycle as shown in Fig. S11b. Therefore, the contribution of the CNT framework to the discharge capacity of A400 electrode could be estimated to be 3.5%.

The excellent lithium-ion storage performance of the fibrous CNTs/MoO_3 composite network was confirmed by electrochemical impedance spectroscopy (EIS) measurements [54–56]. The Nyquist impedance plots of A350, A400, and A500 were obtained via deconvolution with a Randle-type equivalent-circuit model (Fig. S12) before and after 3 and 100 cycles in a fully charged state, as shown in Fig. 7. The Nyquist plots exhibit compressed semicircles in the medium-frequency range, which describe the charge-transfer resistance (Rct) of the electrode [54–56]. The Rct values of the samples were 242, 248, and 191 Ω for A350, A400, and A500, respectively, before cycling (Fig. 7a). The low R_{ct} of A500 is due to the high crystallite size of MoO_3 flat-rods without carbonaceous materials [57–59]. In general, electron scattering in the grain boundary region of the polycrystalline particles increases the charge-transfer resistance. After the third cycle, the R_{ct} values of the samples abruptly decreased to 59 Ω for A350, 39 Ω A400, and 93 Ω for A500, owing to the formation of ultrafine nanocrystals during the initial cycle, as shown in Fig. 7b–d. The R_{ct} values of A350 and A400 are almost identical over the 100 cycles, as shown in Fig. 7b,c. On the other hand, the R_{ct} value of A500

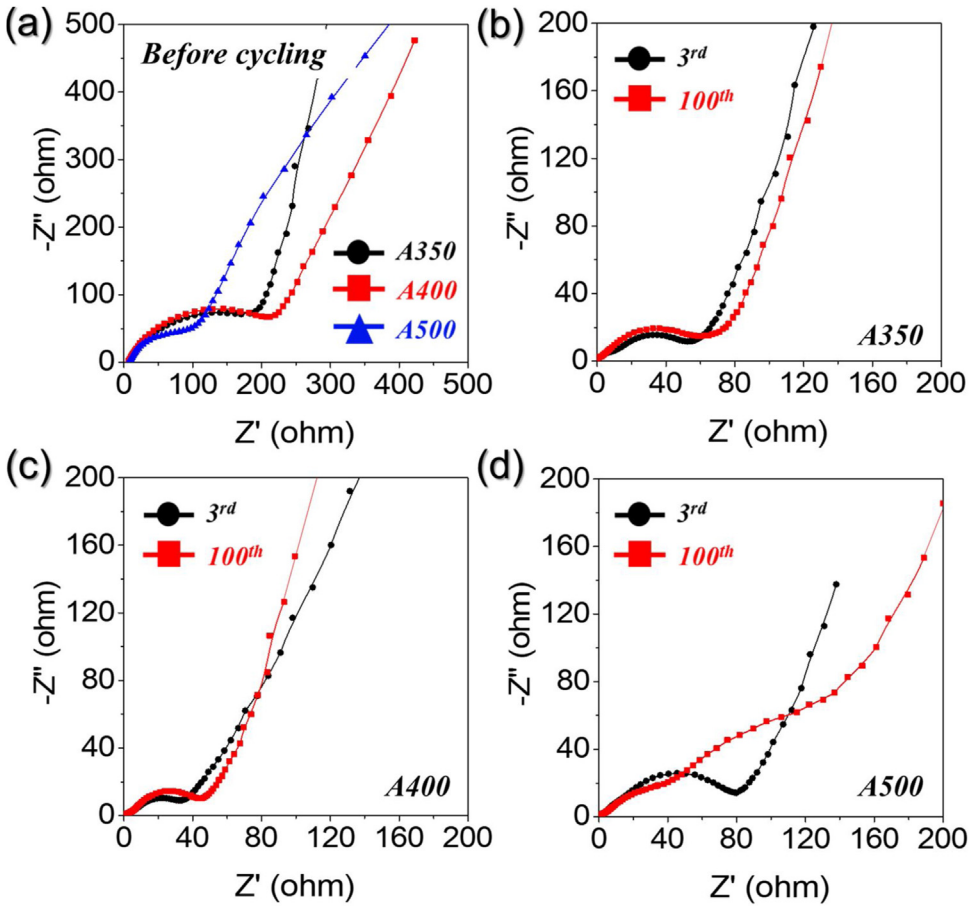

Fig. 7. Nyquist impedance plots of A350, A400, and A500 samples: (a) before cycling, (b) after cycles of A350, (c) after cycles of A400, and (d) after cycles of A500.

increase to 241 Ω after 100 cycles (Fig. 7d), which is due to the structural destruction of MoO_3 flat-rods by the repeated Li^+ ion insertion and desertion processes. The results of the EIS analysis are evidence of the structural stability of the fibrous network of CNTs/MoO_3 composite bundle anchored with MoO_3 nanoplates during the repeated cycles.

Conclusions

In this study, a unique fibrous network of CNTs/MoO_3 composite bundle anchored with MoO_3 nanoplates were prepared by electrospinning process and subsequent simple heat-treatment. In general, it was difficult to synthesize highly integrated and uniformly distributed metal oxide/CNT composite nanofibers because of CNTs aggregation by van der Waals forces and the phase segregation between precursors in a solution, which makes unstable jet during spinning. In this study, by performing the pre-acid-treatments of both CNTs and PAN, dipole-dipole interactions and hydrogen bonding between CNTs and PAN could form $MoO_2(acac)_2$-PAN-CNTs complex in a solution, which allows for the formation of a stable jet during electrospinning. Subsequently, by selectively removing PAN in as-spun fibers during simple heat-treatment, a highly integrated CNTs/MoO_3 bundle network anchored with MoO_3 nanoplates was obtained. The highly integrated CNTs and MoO_3 composite bundle constitute the nanofiber networks and these are efficiently interconnected each other and also contacted with MoO_3 nano-plates. Therefore, the unique CNTs/MoO_3 percolation network makes it possible to achieve a superior lithium ion storage performance by improving electrical conductivity and structure stability.

Declaration of interests

There is no conflict to declare.

Acknowledgements

This work was supported by the National Research Foundation of Korea (NRF) grant funded by the Korea Government (MSIP) (NRF-2018R1A4A1024691, NRF-2017M1A2A2087577, and NRF-2018R1D1A3B07042514).

Appendix A. Supplementary data

Supplementary material related to this article can be found, in the online version, at doi:https://doi.org/10.1016/j.jiec.2019.12.017.

References

[1] M. Jing, J. Wang, H. Hou, Y. Yang, Y. Zhang, C. Pan, J. Chen, Y. Zhu, X. Ji, J. Mater. Chem. A 3 (2015) 16824.
[2] L. Mai, L. Xu, C. Han, X. Xu, Y. Luo, S. Zhao, Y. Zhao, Nano Lett. 10 (2010) 4750.
[3] J. Wang, Q. Zhang, X. Li, D. Xu, Z. Wang, H. Guo, K. Zhang, Nano Energy 6 (2014) 19.
[4] J.S. Cho, Y.J. Hong, Y.C. Kang, ACS Nano 9 (2015) 4026.
[5] J.S. Cho, J.M. Won, J.-K. Lee, Y.C. Kang, Nano Energy 26 (2016) 466.
[6] C. Liang, T. Zhai, W. Wang, J. Chen, W. Zhao, X. Lu, Y. Tong, J. Mater. Chem. A 2 (2014) 7214.
[7] W. Li, L. Zeng, Y. Wu, Y. Yu, Sci. China Mater. 59 (2016) 287.
[8] S.H. Oh, J.-S. Park, M.S. Jo, Y.C. Kang, J.S. Cho, Chem. Eng. J. 347 (2018) 889.
[9] X. Yang, Y. Yang, H. Hou, Y. Zhang, L. Fang, J. Chen, X. Ji, J. Phys. Chem. C 119 (2015) 3923.
[10] Z. Cai, L. Xu, M. Yan, C. Han, L. He, K.M. Hercule, C. Niu, Z. Yuan, W. Xu, L. Qu, Nano Lett. 15 (2014) 738.

[11] X. Wei, W. Li, L. Zeng, Y. Yu, Part. Part. Syst. Char. 33 (2016) 524.
[12] Z. Yan, Q. Hu, G. Yan, H. Li, K. Shih, Z. Yang, X. Li, Z. Wang, J. Wang, Chem. Eng. J. 321 (2017) 495.
[13] Y. Yang, X. Ji, M. Jing, H. Hou, Y. Zhu, L. Fang, X. Yang, Q. Chen, C.E. Banks, J. Mater. Chem. A 3 (2015) 5648.
[14] Y. Wang, G.J. Weng, Micromech. Nanomech. Comp. Solid (2018) 123.
[15] S.H. Oh, O.H. Kwon, Y.C. Kang, J.-K. Kim, J.S. Cho, J. Mater. Chem. A 7 (2019) 12480.
[16] F. Pan, J. Wang, Z. Yang, L. Gu, Y. Yu, RSC Adv. 5 (2015) 77518.
[17] S.H. Yang, S.-K. Park, Y.C. Kang, Chem. Eng. J. 370 (2019) 1008.
[18] S.H. Oh, M.S. Jo, S.M. Jeong, Y.C. Kang, J.S. Cho, Chem. Eng. J. 368 (2019) 438.
[19] B. Zhang, J. Huang, J.K. Kim, Adv. Funct. Mater. 25 (2015) 5222.
[20] W. He, H. Tian, X. Wang, F. Xin, W. Han, J. Mater. Chem. A 3 (2015) 19393.
[21] J. Chen, E. Wang, J. Mu, B. Ai, T. Zhang, W. Ge, L. Zhang, J. Mater. Sci. 54 (2019) 592.
[22] N.T.H. Trang, Z. Ali, D.J. Kang, ACS Appl. Mater. Interfaces 7 (2015) 3676.
[23] L.Q. Mai, B. Hu, W. Chen, Y. Qi, C. Lao, R. Yang, Y. Dai, Z.L. Wang, Adv. Mater. 19 (2007) 3712.
[24] Y. Mao, W. Li, X. Sun, Y. Ma, J. Xia, Y. Zhao, X. Lu, J. Gan, Z. Liu, J. Chen, CrystEngComm 14 (2012) 1419.
[25] J.S. Cho, Nanomaterials 9 (2019) 539.
[26] S.H. Choi, Y.C. Kang, ChemSusChem 7 (2014) 523.
[27] T. Do, H. Lee, Y.G. Ko, Y. Chun, U.S. Choi, C.H. Kim, Colloids Surf. A 514 (2017) 56.
[28] A. Touheed, H. Maab, J. Chin. Chem. Soc. 59 (2012) 1541.
[29] E.V. Basiuk, V.A. Basiuk, J.-G. Bañuelos, J. Phys. Chem. B 106 (2002) 1588.
[30] H.J. Kim, K. Choi, Y. Baek, D.-G. Kim, J. Shim, J. Yoon, J.-C. Lee, ACS Appl. Mater. Interfaces 6 (2014) 2819.
[31] S. Mallakpour, A. Zadehnazari, Carbon 56 (2013) 27.
[32] S. Stankovich, D.A. Dikin, R.D. Piner, K.A. Kohlhaas, A. Kleinhammes, Y. Jia, Y. Wu, S.T. Nguyen, R.S. Ruoff, Carbon 45 (2007) 1558.
[33] Y. Li, J. Zhou, T. Zhang, T. Wang, X. Li, Y. Jia, J. Cheng, Q. Guan, E. Liu, H. Peng, Adv. Funct. Mater. 29 (2019)1808117.
[34] Z. Luo, R. Miao, T.D. Huan, I.M. Mosa, A.S. Poyraz, W. Zhong, J.E. Cloud, D.A. Kriz, S. Thanneeru, J. He, Adv. Energ. Mater. 6 (2016)1600528.
[35] H. Zhang, X. Liu, R. Wang, R. Mi, S. Li, Y. Cui, Y. Deng, J. Mei, H. Liu, J. Power Sources 274 (2015) 1063.
[36] C. Feng, H. Gao, C. Zhang, Z. Guo, H. Liu, Electrochim. Acta 93 (2013) 101.
[37] X.J. Wang, R. Nesper, C. Villevieille, P. Novák, Adv. Energ. Mater. 3 (2013) 606.
[38] K. Crowley, G. Ye, R. He, K. Abbasi, X.P. Gao, ACS Appl. Nano Mater. 1 (2018) 6407–6413.
[39] Z. Li, J. Ma, B. Zhang, C. Song, D. Wang, CrystEngComm 19 (2017) 1479.
[40] G.D. Park, J.-K. Lee, Y.C. Kang, Carbon 128 (2018) 191.
[41] J.-S. Park, Y.C. Kang, J. Mater. Chem. A 5 (2017) 8616.
[42] V. Jadkar, A. Pawbake, R. Waykar, A. Jadhavar, A. Mayabadi, A. Date, D. Late, H. Pathan, S. Gosavi, S. Jadkar, J. Mater. Sci. 28 (2017) 15790.
[43] S.K.S. Patel, K. Dewangan, S.K. Srivastav, N.K. Verma, P. Jena, A.K. Singh, N. Gajbhiye, Adv. Mater. Lett. 9 (2018) 585.
[44] J.S. Cho, S.Y. Lee, Y.C. Kang, Sci. Rep. 6 (2016) 23338.
[45] W. Bai, A. Raghavendra, R. Podila, J.M. Brown, Int. J. Nanomedicine 11 (2016) 4357.
[46] J. Huang, J. Yan, J. Li, L. Cao, Z. Xu, J. Wu, L. Zhou, Y. Luo, J. Alloys Compd. 688 (2016) 588.
[47] U.K. Sen, S. Mitra, Energy Procedia 54 (2014) 740.
[48] Q. Xia, H. Zhao, Z. Du, Z. Zeng, C. Gao, Z. Zhang, X. Du, A. Kulka, K. Świerczek, Electrochim. Acta 180 (2015) 947.
[49] X. Zhang, M. Yang, X. Zeng, Y. Qi, Mater. Lett. 109 (2013) 120.
[50] S. Petnikota, K.W. Teo, L. Chen, A. Sim, S.K. Marka, M.B. Reddy, V.V.S.S. Srikanth, S. Adams, B.V.R. Chowdari, ACS Appl. Mater. Interfaces 8 (2016) 10884.
[51] J.H. Lee, S.H. Oh, S.Y. Jeong, Y.C. Kang, J.S. Cho, Nanoscale 10 (2018) 21483.
[52] M. Yoshio, H. Wang, K. Fukuda, T. Umeno, N. Dimov, Z. Ogumi, J. Electrochem. Soc. 149 (2002) A1598.
[53] Y. Zhu, A. Hu, Q. Tang, S. Zhang, W. Deng, Y. Li, Z. Liu, B. Fan, K. Xiao, J. Liu, X. Chen, ACS Appl. Mater. Interfaces 10 (2018) 8955.
[54] S.H. Oh, J.K. Kim, Y.C. Kang, J.S. Cho, Nanoscale 10 (2018) 18734.
[55] X. Yu, L. Wang, J. Liu, X. Sun, ChemElectroChem 1 (2014) 1476.
[56] G. Zhao, N. Zhang, K. Sun, J. Mater. Chem. A 1 (2013) 221.
[57] I. Bakonyi, V. Isnaini, T. Kolonits, Z. Czigány, J. Gubicza, L. Varga, E. Tóth-Kádár, L. Pogány, L. Péter, H. Ebert, Philos. Mag. 99 (2019) 1.
[58] M.Z. Elias, Physica E 108 (2019) 96.
[59] X. Guo, W. Sigle, J. Fleig, J. Maier, Solid State Ion. 154 (2002) 555.